SUPPLEMENTARY INFORMATION

doi:10.1038/nature18605

1 Supplementary methods

1.1 Model

Wave propagation with frequency ω in a 2D waveguide is described by the complex scattering state $\varphi(x, y, t) = \phi(x, y)e^{-i\omega t}$ satisfying the Helmholtz equation

$$\Delta\phi(x, y) + \varepsilon(x, y)\frac{\omega^2}{c^2}\phi(x, y) = 0 \ , \tag{1}$$

with the speed of light c and the complex dielectric function ε which is modelled by $1 + i\eta/k$ in the waveguide's interior. Here, $k = \omega/c$ denotes the wavenumber. The imaginary part of ε with the dissipation coefficient η describes the losses originating from the interaction with the top and bottom waveguide walls or an absorbing material in the waveguide itself [33]. Note that the 2D model we introduce here is readily applicable to the 3D waveguide employed in the experimental setup if the system resides in the lowest quantized mode between the top and bottom metal plates. As a consequence, the z-axis pointing out of the xy-plane can be neglected, justifying the 2D description (see Supplementary Fig. 1). Furthermore, we emphasize that the applicability of Eq. (1) is not limited to the electromagnetic domain, but may also describe the propagation of, e.g., sound or matter waves.

1.2 Floquet-Bloch picture

In the following we will consider a metallic waveguide, which implies Dirichlet boundary conditions at the waveguide boundary. Considering periodic functions both at the lower and the upper waveguide boundary, at $y = \xi_\downarrow(x)$ and $y = \xi_\uparrow(x)$, respectively, these conditions thus become

$$\phi\big(x, \xi_i(x)\big) = 0 \ , \quad i = \downarrow, \uparrow \ ,$$
$$\xi_\downarrow(x) = \sigma \sin k_b x \quad \text{and} \quad \xi_\uparrow(x) = W + \sigma \sin(k_b x + \vartheta) \ , \tag{2}$$

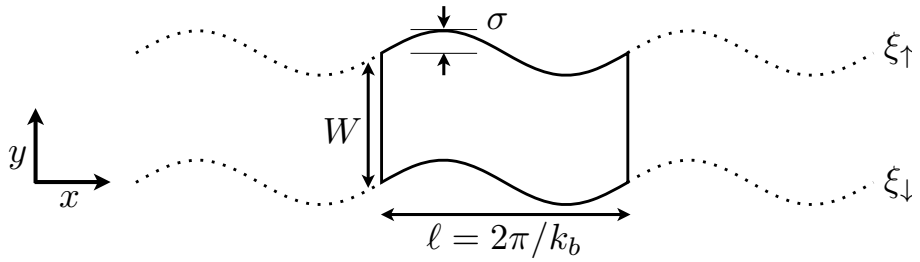

Supplementary Figure 1 | **Waveguide geometry.** A periodic waveguide with width W, boundary wavenumber k_b and undulation amplitude σ. A single unit cell of length $\ell = 2\pi/k_b$ is highlighted by solid lines.

where k_b and σ denote the boundary wavenumber and amplitude, respectively; W is the waveguide width and the constant parameter $\vartheta \in (-\pi, \pi]$ corresponds to the phase shift between the upper and lower boundary. For example, $\vartheta = 0$ corresponds to a periodic waveguide with constant width W (see Supplementary Fig. 1 for an illustration).

In a uniform waveguide, $\sigma = 0$, with no losses, $\eta = 0$, the propagating waves are given by the modes

$$\phi_n(x, y) = \sin\left(\frac{n\pi}{W} y\right) e^{ik_n x}, \quad k_n = \sqrt{k^2 - \left(\frac{n\pi}{W}\right)^2}, \quad n = 1, 2, \ldots \tag{3}$$

We assume that there are only two propagating modes with $n = 1$ and 2, which determine the wavenumber interval as $2 < kW/\pi < 3$. In a periodic waveguide, when $\sigma > 0$, the propagating modes are described by the Bloch solutions

$$\phi(x, y) = \Lambda(x, y)\, e^{iKx}, \tag{4}$$

where $\Lambda(x, y)$ is an x-periodic function with period $\ell = 2\pi/k_b$, i.e., $\Lambda(x + \ell, y) = \Lambda(x, y)$. The Bloch wavenumber K is defined up to an integer multiple of the boundary wavenumber k_b, i.e., $K \pmod{k_b}$. In this work, we study effects related to a degenerate (EP) Bloch wavenumber K, and our first goal is to find values of the parameters corresponding to the EP degeneracy.

1.3 Perturbative approach

To accomplish this task we consider the boundary wavenumber equal to

$$k_b = k_r + \delta\ , \tag{5}$$

where the resonant wavenumber k_r, at which modes 1 and 2 strongly scatter into each other, is given by

$$k_r = k_1 - k_2\ , \tag{6}$$

and δ is the detuning parameter. When $\sigma = \eta = \delta = 0$, we have $k_b = k_r$ and a superposition of the two corresponding modes (3) propagating in the positive x-direction can be written as

$$\phi^0(x, y) = \Lambda^{(0)}(x, y) e^{ik_1 x} \tag{7}$$

with

$$\Lambda^{(0)}(x,y) = a_1 \sin\left(\frac{\pi}{W}y\right) + a_2 \sin\left(\frac{2\pi}{W}y\right) e^{-ik_r x} \tag{8}$$

and arbitrary coefficients a_1 and a_2. Here, the function $\Lambda^{(0)}(x,y)$ is x-periodic with period $\ell_0 = 2\pi/k_r$. Expression (7) can be interpreted as a degenerate Bloch mode of multiplicity two with the wavenumber $k_1 = k_2 \pmod{k_r}$. This is a diabolical point (DP) degeneracy (typical for Hermitian systems) at which only the Bloch wavenumbers merge, while the mode functions remain different, see, e.g., Ref. [1].

In this section, we find the first-order approximation for Bloch modes when the boundary amplitude σ, the detuning parameter δ and the dissipation coefficient η are small quantities of the same order. These Bloch modes are small perturbations of (7) and, thus, can be written in the form (4) with

$$\Lambda(x,y) = \Lambda^{(0)}(x,y) + \Lambda^{(1)}(x,y), \quad K = k_1 + s, \tag{9}$$

where $\Lambda^{(1)}(x,y)$ and s are small corrections of the same order as σ, δ and η, see, e.g., Ref. [34]. Using Eq. (9) in (4), we obtain the Bloch mode in the form

$$\phi(x,y) = [\Lambda^{(0)}(x,y) + \Lambda^{(1)}(x,y) + isx\Lambda^{(0)}(x,y)]e^{ik_1 x}, \tag{10}$$

where the second-order small terms in σ, δ and η and in any of their products were neglected. Substituting (10) into (1) and neglecting again all second-order terms, we get the equation

$$\Lambda^{(1)}_{xx} + 2ik_1\Lambda^{(1)}_x + \Lambda^{(1)}_{yy} + \left(\frac{\pi}{W}\right)^2 \Lambda^{(1)} + 2is(\Lambda^{(0)}_x + ik_1\Lambda^{(0)}) + ik\eta\Lambda^{(0)} = 0\ , \tag{11}$$

with $f_n \equiv \frac{\partial}{\partial n} f$ and $f_{nn} \equiv \frac{\partial^2}{\partial n^2} f$. Note that zero-order terms are canceled in (11) because $\Lambda^{(0)}$ is a solution of the unperturbed problem.

In the first-order approximation, we can transfer the boundary conditions (2) to $y = 0$ and $y = W$ by expanding ϕ in Taylor series as

$$\begin{aligned} 0 &= \phi + \phi_y \sigma \sin k_r x + O(\sigma^2) \quad \text{at} \quad y = 0\ , \\ 0 &= \phi + \phi_y \sigma \sin(k_r x + \vartheta) + O(\sigma^2) \quad \text{at} \quad y = W\ . \end{aligned} \tag{12}$$

Using Eq. (10) in (12), and taking into account that $\Lambda^{(0)} = 0$ at $y = 0$ and W, we obtain

$$\begin{aligned} \Lambda^{(1)} &= -\sigma\Lambda^{(0)}_y \sin k_r x \quad \text{at} \quad y = 0, \\ \Lambda^{(1)} &= -\sigma\Lambda^{(0)}_y \sin(k_r x + \vartheta) \quad \text{at} \quad y = W\ , \end{aligned} \tag{13}$$

where second-order terms were neglected. The function $\Lambda(x,y)$ must be x-periodic with period

$$\ell = \frac{2\pi}{k_b} = \ell_0 + \ell_1\delta + O(\delta^2), \quad \ell_0 = \frac{2\pi}{k_r}, \quad \ell_1 = -\frac{2\pi}{k_r^2}\ . \tag{14}$$

Using Eq. (9), the first-order periodicity condition for $\Lambda(x,y)$ yields

$$\left(\Lambda^{(1)}\right)_{x=0} = \left(\Lambda^{(0)}_x \ell_1 \delta + \Lambda^{(1)}\right)_{x=\ell_0}\ , \tag{15}$$

where we used $\Lambda^{(0)}(x=0,y)=\Lambda^{(0)}(x=\ell_0,y)$. Similarly, the periodicity condition for the derivative Λ_x yields

$$\left(\Lambda_x^{(1)}\right)_{x=0}=\left(\Lambda_{xx}^{(0)}\ell_1\delta+\Lambda_x^{(1)}\right)_{x=\ell_0}\ . \tag{16}$$

The linearized equation (11) can now be solved for s and Λ_0. For this purpose, we multiply it with $\sin\left(\frac{\pi}{W}y\right)$ and integrate with respect to x and y,

$$\begin{aligned}\int_0^W\int_0^{\ell_0}\Big[&\Lambda_{xx}^{(1)}+2ik_1\Lambda_x^{(1)}+\Lambda_{yy}^{(1)}+\left(\frac{\pi}{W}\right)^2\Lambda^{(1)}\\&+2is(\Lambda_x^{(0)}+ik_1\Lambda^{(0)})+ik\eta\Lambda^{(0)}\Big]\sin\left(\frac{\pi}{W}y\right)\mathrm{d}x\mathrm{d}y=0\ .\end{aligned} \tag{17}$$

The first three terms should be integrated using (13), (15) and (16) to get rid of the derivatives of the unknown function $\Lambda^{(1)}$. The resulting terms containing $\Lambda^{(1)}$ cancel out, yielding the equation

$$\begin{aligned}0=&\int_0^W\int_0^{\ell_0}\left[2is\left(\Lambda_x^{(0)}+ik_1\Lambda^{(0)}\right)+i\eta k_b\Lambda^{(0)}\right]\sin\left(\frac{\pi}{W}y\right)\mathrm{d}x\mathrm{d}y\\&-\ell_1\delta\int_0^W\left[\Lambda_{xx}^{(0)}(\ell_0,y)+2ik_1\Lambda_x^{(0)}(\ell_0,y)\right]\sin\left(\frac{\pi}{W}y\right)\mathrm{d}y\\&-\sigma\frac{\pi}{W}\int_0^{\ell_0}\left[\Lambda_y^{(0)}(x,W)\sin\left(k_rx+\vartheta\right)+\Lambda_y^{(0)}(x,0)\sin\left(k_rx\right)\right]\sin\left(\frac{\pi}{W}y\right)\mathrm{d}x\ .\end{aligned} \tag{18}$$

Then, using the explicit form of $\Lambda^{(0)}$ from (8) and of ℓ_0 and ℓ_1 from (14) yields, dropping a common factor of $k_r/\left(2\pi Wk_1\right)$,

$$\left(\frac{i\eta}{2}\frac{k}{k_1}-s\right)a_1+i\frac{\sigma}{k_1}(e^{i\vartheta}+1)\frac{\pi^2}{W^3}\,a_2=0\ . \tag{19}$$

A similar integration using the factor $\sin\left(\frac{2\pi}{W}y\right)e^{ik_rx}$ instead of $\sin\left(\frac{\pi}{W}y\right)$ in Eq. (17), yields

$$-i\frac{\sigma}{k_2}(e^{-i\vartheta}+1)\frac{\pi^2}{W^3}\,a_1+\left(\delta+i\frac{\eta}{2}\frac{k}{k_2}-s\right)a_2=0\ . \tag{20}$$

A nontrivial solution (a_1,a_2) of system (19) and (20) exists if and only if the determinant vanishes, i.e.,

$$\left(s-i\frac{\eta}{2}\frac{k}{k_1}\right)\left(s-\delta-i\frac{\eta}{2}\frac{k}{k_2}\right)-\frac{2\pi^4}{W^6}\frac{\sigma^2}{k_1k_2}\left(1+\cos\vartheta\right)=0\ . \tag{21}$$

The roots s of this equation and the corresponding solution (a_1,a_2) determine the corrections to the Bloch modes in Eqs. (4), (8) and (9). Note that, in the absence of dissipation, $\eta=0$, our analysis fully reproduces the results obtained in Ref. [35].

1.4 Effective 2×2 model

In the next step, we derive the effective two-level Schrödinger equation corresponding to the propagation of the two nearly resonant Bloch modes. For this purpose, we write the solution (4) given by (8) and (9) as

$$\phi(x,y) \approx \big(a_1\phi_1(x,y) + a_2\phi_2(x,y)\big)e^{isx} , \tag{22}$$

where the coefficients

$$\begin{aligned} c_1(x) &= a_1\sqrt{k_1}e^{i(\pi-\vartheta)/4}e^{-i(\delta-s)x} , \\ c_2(x) &= a_2\sqrt{k_2}e^{-i(\pi-\vartheta)/4}e^{-i(\delta-s)x} , \end{aligned} \tag{23}$$

satisfy the Schrödinger equation

$$i\frac{\partial}{\partial x}\begin{pmatrix} c_1 \\ c_2 \end{pmatrix} = H\begin{pmatrix} c_1 \\ c_2 \end{pmatrix} , \quad H = \begin{pmatrix} \delta - i\frac{\eta}{2}\frac{k}{k_1} & B\sigma \\ B\sigma & -i\frac{\eta}{2}\frac{k}{k_2} \end{pmatrix} , \tag{24}$$

with

$$B = \sqrt{2\,(1+\cos\vartheta)}\,\frac{\pi^2}{W^3}\,\frac{1}{\sqrt{k_1k_2}} . \tag{25}$$

The eigenvalue E of the Hamiltonian (24) is related to the Bloch wavenumber K via Eq. (23) and Eqs. (5), (6) and (9) as

$$E = \delta - s = \delta + k_1 - K = k_b + k_2 - K . \tag{26}$$

So far, we have considered a uniform dissipation with a constant parameter η. To engineer the waveguide's mode-dependent transmission such that one mode suffers large loss, while the other mode propagates (approximately) undamped, we now extend the model to allow absorption that is distributed non-uniformly along the waveguide.

Manipulating loss in a waveguide design implies, however, that the loss parameter is position-dependent, $\eta = \eta(x,y)$. In order to keep the Floquet-Bloch formalism valid, we consider periodic losses with the period of the boundary modulation $\ell = 2\pi/k_b$, i.e.,

$$\eta = \eta_0\tilde{\eta}(x,y), \quad \tilde{\eta}(x+\ell,y) = \tilde{\eta}(x,y) , \tag{27}$$

where $\tilde{\eta}(x,y)$ is a given function describing the loss distribution and the real parameter η_0 controls the loss intensity. Performing the derivation as for uniform absorption, integrals of the form

$$\Gamma_{nm} = \frac{e^{i(\pi-\vartheta)(m-n)/2}}{\pi W}\frac{kk_b}{\sqrt{k_nk_m}}\int_0^\ell\!\!\int_0^W \tilde{\eta}(x,y)\sin\left(\frac{n\pi}{W}y\right)\sin\left(\frac{m\pi}{W}y\right)e^{-i(k_n-k_m)x}\mathrm{d}x\mathrm{d}y \tag{28}$$

now appear, leading to the Hamiltonian

$$H = \begin{pmatrix} \delta & B\sigma \\ B\sigma & 0 \end{pmatrix} - i\frac{\eta_0}{2}\begin{pmatrix} \Gamma_{11} & \Gamma_{12} \\ \Gamma_{12}^* & \Gamma_{22} \end{pmatrix} . \tag{29}$$

Note that we have changed the integration limit from ℓ_0 to ℓ and k_r to k_b in Eq. (28), which is justified within a first order perturbation approach, taking into account the exact

period of the boundary modulation. In case of constant losses, i.e., $\tilde{\eta}(x,y)=1$, we obtain $\Gamma_{n\neq m}=0$ and $\Gamma_{nn}=\frac{k}{k_n}$, returning to Eq. (24).

A very efficient way to engineer the mode-specific absorption is to choose its spatial distribution according to the Hermitian dyadic product $v_2 v_2^\dagger$. Here, v_2 is one of the two eigenvectors of the system in the absence of absorption, with eigenvalue E_2, i.e.,

$$H_0 v_2 = E_2 v_2 \ , \quad H_0 = \begin{pmatrix} \delta & B\sigma \\ B\sigma & 0 \end{pmatrix} \ . \tag{30}$$

Introducing the composite Hamiltonian,

$$H = H_0 - i\frac{\eta}{2} v_2 v_2^\dagger \ , \tag{31}$$

with the anti-Hermitian dissipative term $-i\frac{\eta}{2}v_2 v_2^\dagger$, one can see that the first eigenstate v_1 does not dissipate at all due to the orthogonality condition $v_2^\dagger v_1 = 0$, in contrast to the second eigenstate v_2 leading to a decay rate $\propto \exp\left(-\frac{\eta}{2}x\right)$. In fact, this procedure is the optimal way in which a dissipation asymmetry for a 2-mode system can be introduced.

While the dyadic form of Γ_{nm} for the losses in the effective 2×2 description is very efficient, we also tested the results for the case when placing the absorbing material just close to the nodes of the second mode, and found this approach to work very well (especially in view of practical demands of the experiment). Eventually we also implemented this latter protocol in the experimental microwave setup (see Fig. 3a,b in the main text and section 1.8 below).

1.5 EP structure

The Hamiltonian in Eq. (1) presented in the main text is obtained from Eq. (24) by identifying $g = B\sigma$ and $\gamma_n = \eta k/k_n$, $n = 1, 2$. It possesses the eigenvalue spectrum

$$E_{1,2} = \frac{\delta}{2} - i\frac{\gamma_1+\gamma_2}{4} \pm \frac{1}{2}\sqrt{\Delta} \ , \quad \Delta \equiv \left(\delta - i\frac{\gamma_1-\gamma_2}{2}\right)^2 + 4g^2 \ . \tag{32}$$

The degenerate state $E_1 = E_2$ appears when both the real and imaginary part of Δ vanish simultaneously, yielding

$$g_{\rm EP} = \pm\frac{|\gamma_1-\gamma_2|}{4} \ , \quad \delta_{\rm EP} = 0 \ . \tag{33}$$

When $\eta > 0$, we have $\gamma_1 \neq \gamma_2$ and there is a single eigenvector $v_{\rm EP} \propto (1, \pm i)^T$ of the Hamiltonian (24), meaning that Eq. (33) defines an EP degeneracy where both eigenvalues and eigenvectors of the Hamiltonian coincide. Therefore, in the first approximation, the EP degeneracy appears for the waveguide with periodic boundary of amplitude $\sigma = g_{\rm EP}/B$ and resonant wavenumber $k_b = k_r$.

1.6 Dynamically encircling an EP in a waveguide

Using the model system (24), we now investigate the transmission through a waveguide for which the boundary modulation and the loss parameter change slowly along the

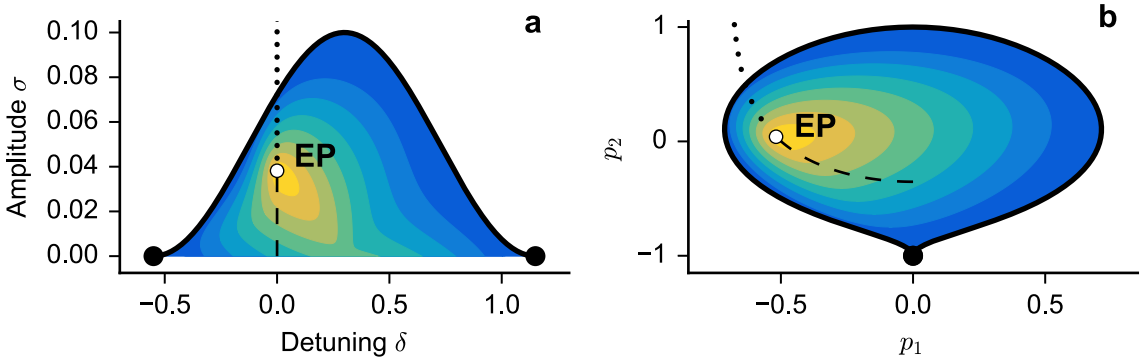

Supplementary Figure 2 | **Parameter-space trajectory. a**, The path in Eq. (34) is shown here in parameter space (δ, σ) as a black solid line. The EP is indicated by a white point. Black dots denote the start and end points of the parameter trajectory, corresponding to identical waveguides of uniform width. The respective lines where $\mathrm{Re}E_1 = \mathrm{Re}E_2$ and $\mathrm{Im}E_1 = \mathrm{Im}E_2$ are shown by dashed and dotted lines, respectively. The following set of values has been used to determine the waveguide parameters through Eq. (34): $L/W = 100$, $kW/\pi = 2.05$, $\sigma_0/W = 0.1$, $\delta_0 W = 0.85$, $\rho W = 0.3$, $\eta_0 W = 0.6$. **b**, Here we show the same path as in **a**, but in a different parameter space (p_1, p_2), in which each point corresponds to a unique waveguide realization and in which the states at the start and end points coincide at a single point, $p_1 = 0$ and $p_2 = -1$. With these new parameters it becomes immediately apparent that our parameter-space trajectory, indeed, forms a closed loop around the EP. Colors indicate how also other loops or areas transform into each other. Note that the dashed line would extend to the black dot along the line $p_1 = 0$ ($\sigma = 0$ in panel **a**) when the above equality $[\mathrm{Re}E_1 = \mathrm{Re}E_2]$ is extended to its Floquet-Bloch form $[\mathrm{Re}E_1 = \mathrm{Re}E_2 \ (\mathrm{mod}\, k_b)]$, see section 1.7 for a corresponding discussion.

propagation-axis x (for an illustration we refer to Fig. 2e in the main text). Specifically, we choose the following parametrization for the parameter evolution,

$$\begin{aligned} \sigma(x) &= \frac{\sigma_0}{2}\left(1 - \cos\frac{2\pi}{L}x\right) , \\ \delta(x) &= \delta_0\left(2\frac{x}{L} - 1\right) + \rho , \\ \eta(x) &= \frac{\eta_0}{4}\left(1 - \cos\frac{2\pi}{L}x\right)^2 , \end{aligned} \tag{34}$$

where $0 \leq x \leq L$, with the finite waveguide length $L \gg \ell$. Note that it is well justified to move from an infinitely extended system to a finite one if the parameter variations over a distance $\ell \ll L$ are small. The constants σ_0 and δ_0 determine the maximum roughness and detuning strengths of the boundary $\xi(x)$, respectively, η_0 denotes the dissipation strength and ρ corresponds to a constant detuning offset. Values of these parameters used in the simulations are given in the captions of Supplementary Figs. 3 and 5.

We emphasize that the systems realized at positions $x = 0$ and $x = L$ are identical, since both correspond to a uniform waveguide without absorption. A waveguide with

parameters (34) therefore emulates a closed loop in parameter space and we will show that this loop encircles an EP. To facilitate this, let us consider the plane (δ, σ), in which the parameter trajectory (34) is presented in Supplementary Fig. 2a by a solid black curve and its and its start and end points by black dots. For arbitrary δ and σ, we choose the Hamiltonian (24) with the damping parameter

$$\eta = \frac{\eta_0}{4}\left[1+\cos\left(\pi\frac{(\delta-\rho)}{\delta_0}\right)\right]^2 , \tag{35}$$

providing an extension from the loop (34) to the whole (δ, σ)-plane. Using Eq. (33) with $g = B\sigma$ and $\gamma_i = \eta k/k_i$, one finds that there is a single EP corresponding to

$$\delta_{\rm EP} = 0 \ , \quad \sigma_{\rm EP} = \frac{|\gamma_1-\gamma_2|}{4B} = \frac{\eta_0}{16B}\left[1+\cos\left(\pi\frac{\rho}{\delta_0}\right)\right]^2\left|\frac{k}{k_1}-\frac{k}{k_2}\right| , \tag{36}$$

shown by a white dot in Supplementary Fig. 2a. There are two lines at which either the real or the imaginary part of the energies $E_{1,2}$ coincide, starting at the EP in opposite directions: the one line corresponding to equal energies ${\rm Re}E_1 = {\rm Re}E_2$ is shown by a dashed curve, while the other line, given by equal widths, i.e., ${\rm Im}E_1 = {\rm Im}E_2$, is indicated by a dotted curve.

To assure ourselves that the loop (34) indeed encircles the EP (the white dot) we note that the two parameters (σ, δ) determine a specific waveguide geometry through the boundary function $\xi(x) = \sigma\sin(k_r+\delta)x$. For vanishing amplitude, $\sigma = 0$, we have a rectangular waveguide, $\xi(x) = 0$, such that all waveguide configurations with an arbitrary detuning δ are identical. When adding the losses according to the coefficient η in Eq. (34), the configurations at x and $L-x$ still correspond to exactly the same physical system, since $\eta(x) = \eta(L-x)$. Hence, the two black points in Supplementary Fig. 2a (the initial and final states of the parameter trajectory) characterize the same waveguide configuration and the black line connecting them corresponds to a closed loop around the EP.

To see this in a more straightforward way, we remove the ambiguity involved in this parametrization by transforming (σ, δ) to a new set of parameters (p_1, p_2),

$$p_1(\sigma,\delta) = r(\sigma,\delta)\sin 2\alpha(\sigma,\delta) , \tag{37}$$

$$p_2(\sigma,\delta) = r(\sigma,\delta)\cos 2\alpha(\sigma,\delta) , \tag{38}$$

with

$$r(\sigma,\delta) = \sqrt{\left(\frac{\sigma}{\sigma_0}\right)^2+\left(\frac{\delta-\rho}{\delta_0}\right)^2} , \tag{39}$$

$$\alpha(\sigma,\delta) = \arctan\left(\frac{\delta-\rho}{\delta_0}\Big/\frac{\sigma}{\sigma_0}\right) . \tag{40}$$

These parameters (p_1, p_2) have the advantageous property that they determine a waveguide system uniquely in the sense that no other parameter pair (p_1, p_2) corresponds to the same waveguide realization. For this alternative parameter set it now becomes immediately apparent also visually (see Supplementary Fig. 2b), that our parametrization in

Eq. (34) describes a closed loop around the EP. We want to emphasize that, mathematically, one may in principle map an arbitrary open path to a closed one by an appropriate transformation. Such a mapping is, however, only meaningful if systems which are physically identical are mapped onto the same point in parameter space.

Furthermore, we note that in terms of the Bloch-Floquet picture employed in this work, (σ, δ) are a natural choice of physical parameters, such that we will continue to work with them in the following, while keeping in mind that our protocol indeed involves the full encircling of an EP.

1.7 Asymmetric mode-switch in a waveguide with absorption

A central theme of our work is that one must distinguish between a *parametric* and a *dynamical* encircling of an EP. In the former case, we follow the change of eigenstates continuously along the loop, while in the latter case the parameters change slowly in time (here, in longitudinal direction x), and we follow the true solution of the time-dependent Schrödinger equation (24).

The instantaneous eigenvalues $E_i(x)$ and the (right) eigenvectors $\Phi_i(x)$ satisfy

$$H(x)\Phi_i(x) = E_i(x)\Phi_i(x) \ , \qquad i = 1, 2 \ , \tag{41}$$

and we impose the normalization condition $|\Phi_i(x)|^2 = \Phi_i^\dagger(x)\Phi_i(x) = 1$. Here, the time (or position) x plays the role of a parameter. The fact that the EP is encircled parametrically by the loop leads to a state-flip if the eigenvectors $\Phi_i(x)$ are defined continuously dependent on x:

$$\begin{aligned} \text{mode } 1 &= \Phi_1(0) = \Phi_2(L) \ , \\ \text{mode } 2 &= \Phi_2(0) = \Phi_1(L) \ . \end{aligned} \tag{42}$$

Within the above framework, a *parametric* encircling around the EP (traversing the loop in Supplementary Fig. 2 from left to right) turns one instantaneous eigenvector continuously into the other, i.e.,

$$\circlearrowright\text{: mode } 1 = \Phi_1(0) \to \Phi_1(L) = \text{mode } 2 \ , \tag{43}$$

$$\circlearrowright\text{: mode } 2 = \Phi_2(0) \to \Phi_2(L) = \text{mode } 1 \ . \tag{44}$$

The same happens when traversing the loop in the opposite direction (from right to left):

$$\circlearrowleft\text{: mode } 1 = \Phi_2(L) \to \Phi_2(0) = \text{mode } 2 \ , \tag{45}$$

$$\circlearrowleft\text{: mode } 2 = \Phi_1(L) \to \Phi_1(0) = \text{mode } 1 \ , \tag{46}$$

realizing a symmetric switch of the initial states $\Phi_{1,2}(0)$ and final states $\Phi_{1,2}(L)$. Here, an additional Berry phase factor appears which we ignore since it is of no relevance for the present work.

The corresponding parameter-dependent eigenvalues $E_i(x)$ are shown in Supplementary Fig. 3. Note that at the endpoints $x = 0$ and $x = L$, the eigenvalues E_i are brought together again, i.e., $E_1(0) = E_2(L)$ and $E_1(L) = E_2(0)$, if we recall from Eq. (4) that K, and thus the eigenvalue E, is only determined mod k_b. Here we take

into account that k_b has an x-dependence as well, $k_b(x) = k_r + \delta(x)$, see Eq. (5). Directly at the loop endpoints, both the roughness $\sigma(x)$ and dissipation $\eta(x)$ vanish, with the eigenvalues $E_i(x)$ then being given by $\delta(x)$ and 0. Thus, $E_2(0) - E_1(L) = 0$ and $E_2(L) - E_1(0) = \delta(L) - \delta(0) = k_b(L) - k_b(0)$, i.e., the respective eigenvalues coincide at $x = 0$ and $x = L$ due to the underlying Floquet-Bloch picture (see the dashed lines and the arrow in Supplementary Fig. 3).

The above symmetric switching between states $\Phi_{1,2}$ is, however, not what happens when encircling an EP *dynamically*. Upon a numeric integration of Eq. (24) following the path defined in Eq. (34), we expand the solution vector in the instantaneous eigenbasis Eq. (41) as

$$\psi(x) \equiv \begin{pmatrix} c_1(x) \\ c_2(x) \end{pmatrix} = b_1(x)\Phi_1(x) + b_2(x)\Phi_2(x) \ . \tag{47}$$

Despite the flip of the instantaneous eigenvectors, the solution $\psi(x)$ initialized in one of the eigenmodes Φ_i generally follows the adiabatic prediction $b_i^{\mathrm{ad}}(x) \sim \exp\left(-i\int_0^x E_i(x')\mathrm{d}x'\right)$ only for one specific encircling direction if transported truly dynamically around the EP. The condition for this to happen (given in Ref. [18]) requires the non-adiabatic contribution to be small, and it is satisfied if the loop remains most of the time on the energy sheet of the longest lived state (see, also, Fig. 1a,b in the main text). For the other eigenmode, strong non-adiabatic effects appear, such that the state does not follow the instantaneous eigenvector but rather returns to itself, apart from some prefactor (see, e.g., Ref. [14]). If the encircling direction is reversed, the inverse behaviour is found: the eigenstate that evolved adiabatically before now undergoes non-adiabatic transitions due to the system's non-Hermiticity, while the other eigenmode follows the adiabatic prediction (see the right column of Supplementary Fig. 4). This means that, depending on the input direction, a specific dominating mode is obtained, realizing an asymmetric switch between the eigenmodes.

Results. In Supplementary Fig. 4 we show the real eigenvalues $E_i(x)$ weighted by the respective eigenvector populations $|b_i(x)|^2$,

$$P(x) \equiv \frac{\mathrm{Re}E_1(x)|b_1(x)|^2 + \mathrm{Re}E_2(x)|b_2(x)|^2}{|b_1(x)|^2 + |b_2(x)|^2} \ , \tag{48}$$

for different initial conditions and encircling directions. When describing a loop around the EP in a counter-clockwise direction (which we identify with injection in the waveguide from the left), states initialized in either the first mode (red dashed line in Supplementary Fig. 4a) or in the second mode (blue dashed line Supplementary Fig. 4a) result in a population $|b_2(L)|^2$ that is much larger than the corresponding population $|b_1(L)|^2$, such that $P(x)$ from Eq. (48) follows closely the upper ($\mathrm{Re}E_2$) eigensheet. This corresponds to the first mode being dominant at the end of the waveguide at $x = L$ for both initial conditions:

$$\begin{aligned} \circlearrowleft&: \text{mode } 1 = b_1(0)\Phi_1(0) \to b_2(L)\Phi_2(L) = \text{mode } 1 \ , \\ \circlearrowright&: \text{mode } 2 = b_2(0)\Phi_2(0) \to b_2(L)\Phi_2(L) = \text{mode } 1 \end{aligned} \tag{49}$$

Upon reversing the encircling direction (trajectories now start at $x = L = 100$ and propagate leftwards to the final position $x = 0$, see Supplementary Fig. 4b), both initial

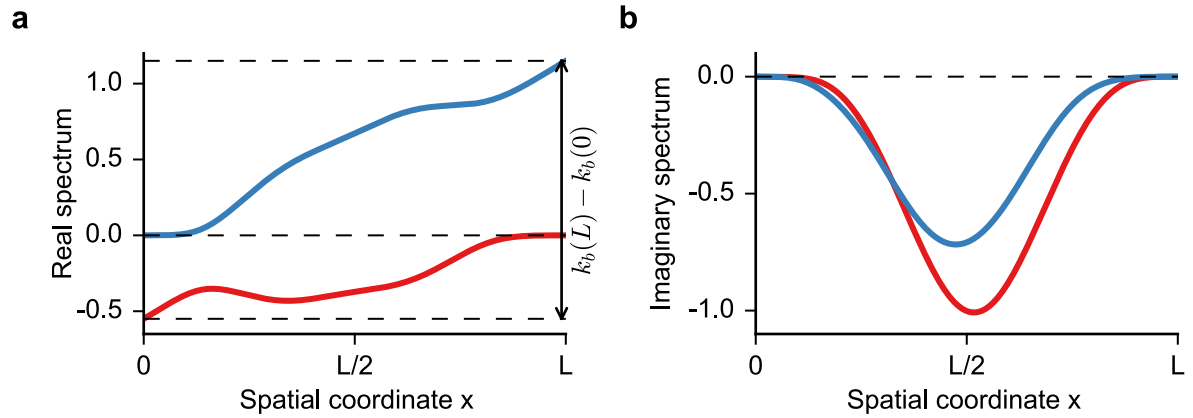

Supplementary Figure 3 | **Parameter-dependent eigenvalue spectrum for bulk absorption.** **a**, Real part of the parameter-dependent eigenvalue spectrum $E_{1,2}(x)$ Eq. (32), parametrized according to Eq. (34) (shown by solid lines). The coloring is such that red (blue) corresponds to the eigenvalue of the first (second) eigenstate at the beginning of the evolution at $x = 0$. **b**, Imaginary part of the spectrum. Here we employ a loss potential which is uniform in y-, and slowly varying in x-direction. Dashed lines indicate that the spectrum at the loop endpoints $x = 0$ and $x = L$ differs only by integer multiples of $k_b(0)$ and $k_b(L)$ in the employed Floquet-Bloch picture (we refer to the text for more details). The corresponding model parameters can be found in the caption of Supplementary Fig. 2.

states yield a much higher population for $|b_2(0)|^2$,

$$\circlearrowleft\text{: mode } 1 = b_2(L)\Phi_2(L) \to b_2(0)\Phi_2(0) = \text{mode } 2\ ,$$

$$\circlearrowright\text{: mode } 2 = b_1(L)\Phi_1(L) \to b_2(0)\Phi_2(0) = \text{mode } 2\ . \tag{50}$$

Thus, the system ends in a different final state Φ_2 as compared to Eqs. (49).

Furthermore, we want to emphasize that with a dissipation like in Eq. (35), both eigenstates experience equal dissipation at the start and end of the parameter trajectory, i.e., with $\mathrm{Im}E_1 = \mathrm{Im}E_2$ (see Supplementary Figs. 3b and 12a). In this way a loop is realized that avoids multiple non-adiabatic flips during the evolution. See, e.g., Refs. [15,16,21] for a study on the consequences of different starting points in parameter space on the dynamics.

With this example we have already demonstrated the basic principle of the asymmetric switching device: suppose that a superposition of two modes is injected from the left and from the right. Due to the EP encircling induced by the spatial variation of the boundary amplitude and frequency (in the presence of loss), the initial state will result in different dominating pure modes at the end of the loop, depending only on the encircling direction. In the waveguide setup, this leads to a mode-selection depending on the direction from which the state is injected. With the boundary parametrization Eq. (34), our concept can be readily applied to the actual waveguide system (see Figs. 2 and 3 in the main text, as well as Supplementary Fig. 11).

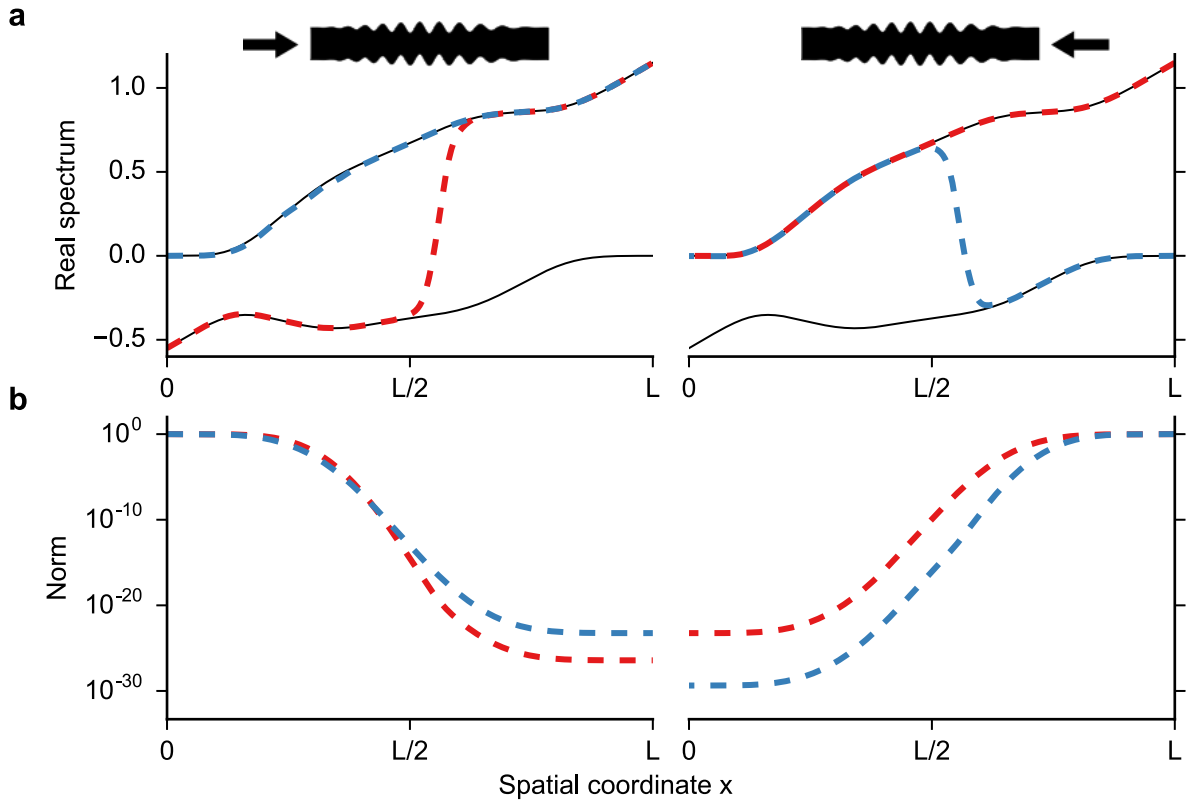

Supplementary Figure 4 | **Dynamically encircling an EP in a waveguide with bulk absorption.** Counter-clockwise loops correspond to injection from the left (starting at $x = 0$, left column), clockwise loops correspond to injection from the right (starting at $x = L$, right column), see also the insets at the top. **a**, Position-dependent eigenvalue spectrum $E_{1,2}(x)$ (shown by black lines, corresponding to the data shown in Supplementary Fig. 3), as well as $P(x)$, the real eigenvalue spectrum weighted by the respective eigenvector populations $|b_i(x)|^2$, shown in dashed colored lines. The coloring of $P(x)$ corresponds to the initial condition: Red (blue) corresponds to the state being injected in the first (second) eigenmode, for injection from the right the coloring is reversed since the instantaneous eigenmodes are flipped. The x position at which non-adiabatic transitions occur is located approximately at $x = L/2$, where $P(x)$ departs from the eigenvalue surface it initially follows [21]. **b**, The norm $|b_1(x)|^2 + |b_2(x)|^2$, showing the magnitude of the overall decay for trajectories of the same color as in panel **a**. The corresponding model parameters can be found in the caption of Supplementary Fig. 2.

1.8 Asymmetric mode-switch in a waveguide with position dependent absorption

It is evident from Supplementary Fig. 4b, where we plot the norm of the propagating state ψ, that the device quality is strongly limited by the large absorption both propagating modes suffer from, leading to a decay by many orders of magnitude. For uniform absorption, this behavior is impossible to overcome: To induce a non-adiabatic transition during an EP encircling, the system size L and/or the absorption strength η have to be large. A

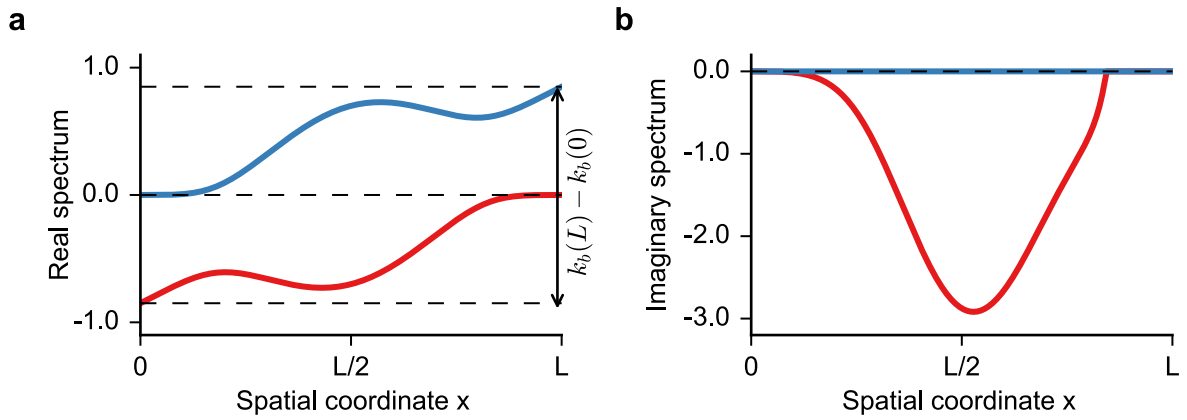

Supplementary Figure 5 | Parameter-dependent eigenvalue spectrum for position dependent absorption. Here we show the same as in Supplementary Fig. 3, with the difference that we are now employing position dependent absorption in the waveguide setup. Note that the respective imaginary part of the eigenvalue, Im E_n, is almost zero for one mode, while it is very large for the other. The following set of values has been used to determine the waveguide parameters through Eq. (34): $L/W = 100$, $kW/\pi = 2.05$, $\sigma_0/W = 0.1$, $\delta_0 W = 0.85$, $\rho W = 0.0$, $\eta_0 W = 1.0$.

reduction of either of the two quantities inevitably reduces the quality of the whole mode-selection scheme. Also, the relative dissipation strength of both modes, $|\gamma_1 - \gamma_2|$, is largest directly at the mode-opening $k \approx 2\pi/W$, where the wavenumber k_2 is much smaller than k_1 (see Eq. (3)). As shown in section 1.4, these problems can be conveniently solved by introducing non-uniform absorption in the waveguide, which removes the absorption of one eigenmode and simultaneously increases the losses for the second considerably.

The non-uniform absorption is facilitated by identifying the nodes of the wavefunction $\phi(x, y)$ in Eq. (22) obtained for a system with no absorption, $\eta_0 = 0$, and placing absorbers at the node positions (e.g., of Gaussian shape), yielding the loss distribution $\tilde{\eta}(x, y)$ which in turn determines Γ_{nm} in Eq. (28). In Supplementary Fig. 5 we plot the corresponding spectrum, where the imaginary part ImE_i now differs decisively from the system shown in Supplementary Fig. 3: Now, the imaginary part of the eigenvalue is close to zero for one mode, while the other mode exhibits a very large absorption.

One can immediately appreciate the benefit of the above strategy by comparing the results in Supplementary Fig. 6 with Supplementary Fig. 4: Injected from the left, one mode propagates adiabatically and approximately undamped, the other mode however is strongly dissipated while traversing the undulated waveguide and undergoes the non-adiabatic transition to the first mode. By way of this, we have realised a high-quality asymmetric switch that is based on the injection direction.

Furthermore, the designed absorber placement makes it possible to greatly reduce the device dimensions to lengths considerably smaller than a length-to-width ratio of $L/W = 100$, up to the limit at which additional non-adiabatic contributions inevitably set in due to the fast evolution.

To obtain the EP position, it is necessary to extend the Hamiltonian from the pa-

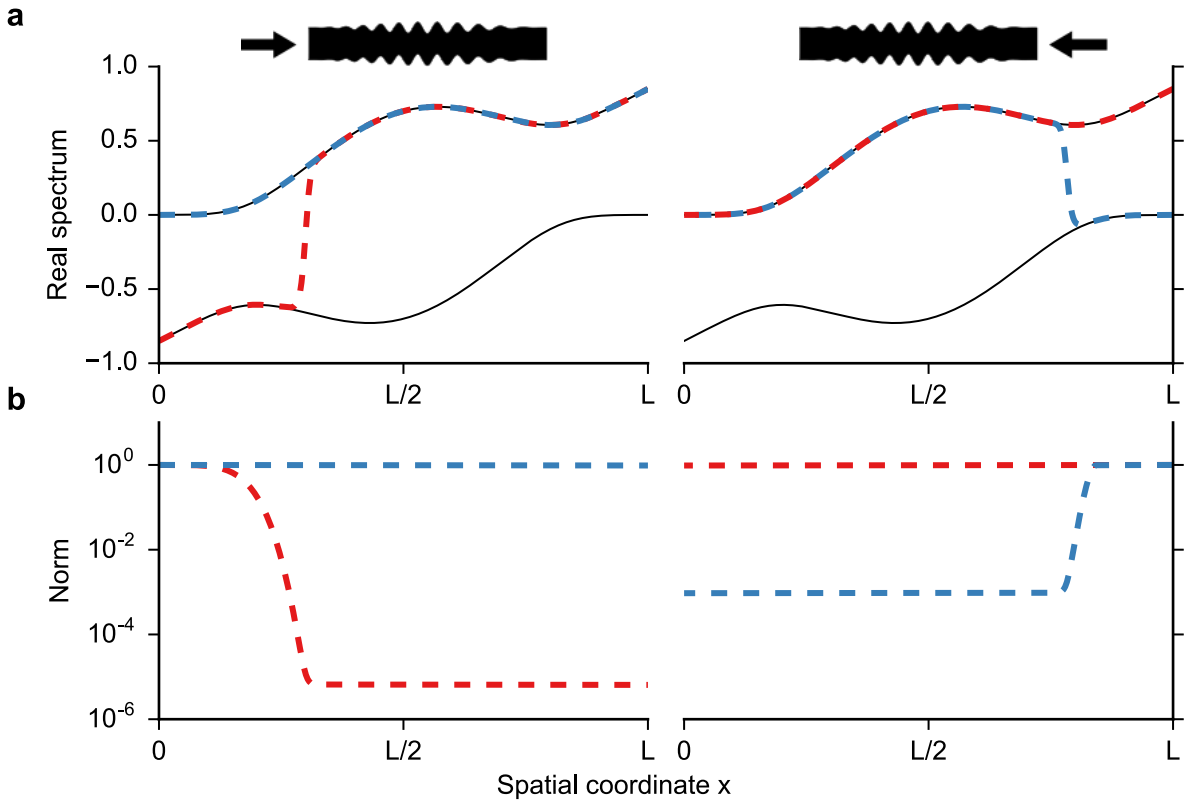

Supplementary Figure 6 | **Dynamically encircling an EP in a waveguide with position dependent absorption.** Here we show the same as in Supplementary Fig. 4, with the difference that we are now employing position dependent absorption in the waveguide setup. The corresponding model parameters can be found in the caption of Supplementary Fig. 5.

rameter trajectory to the inside of the loop, i.e., to extend the spectrum from the path $(\delta(x), \sigma(x))$ to all other points in the (δ, σ)-plane, and to show that the EP is encircled in the process. To extend the Hamiltonian, we choose

$$H(\sigma, \delta) = H_0 - i\frac{\eta_0}{2}\tilde{\Gamma}(\sigma, \delta) \ , \tag{51}$$

with

$$H_0 \equiv \begin{pmatrix} \delta & B\sigma \\ B\sigma & 0 \end{pmatrix} \ , \quad \tilde{\Gamma}(\sigma, \delta) \equiv \begin{pmatrix} \frac{k}{k_1} & 0 \\ 0 & \frac{k}{k_2} \end{pmatrix} \Delta_\sigma + (1 - \Delta_\sigma) \left(\frac{\sigma}{\sigma_0}\right)^2 \Gamma\left(f(\delta), \delta\right) \ , \tag{52}$$

$$f(\delta) \equiv \frac{1}{4}\left[1 + \cos\left(\pi \frac{(\delta - \rho)}{\delta_0}\right)\right]^2 \ , \quad \Delta_\sigma \equiv f(\delta) - \left(\frac{\sigma}{\sigma_0}\right)^2 \ , \tag{53}$$

which interpolates between position dependent absorption at the parameter loop and a uniform dissipation at $\sigma = 0$. Here, the function $\Gamma(\sigma, \delta)$ denotes the matrix Γ_{nm} which is based on the node positions of Eq. (22), which in turn depends on $H_0 = H_0(\sigma, \delta)$ (i.e.,

the waveguide system in the absence of dissipation, $\eta_0 = 0$). In the above extension of the Hamiltonian, Γ depends only on δ, $\Gamma = \Gamma(f(\delta), \delta)$. The procedure to show that an EP is encircled is analogous to the uniform absorption case, we thus refer here to section 1.6 for this argument. Here, we resort to obtaining the EP position numerically, since the analytic expressions are cumbersome and do not offer any additional insight (see Supplementary Fig. 12b).

Note that one has ample freedom in choosing the absorber position while still retaining the asymmetric switching effect. The most effective strategy relies on placing the absorbers directly at the modal node positions, as used for the effective model calculations shown above. For the experimental realization of the waveguide system, however, such a loss placement would result in undesirably large back-reflections in the waveguide. To mitigate this shortcoming, we thus rely on a continuous stripe-absorber to obtain the decay necessary to encircle the EP, although it comes at the expense of an additional parasitic absorption for the other, previously undamped, mode. However, as we show in the main text (see Fig. 3), this alternative absorber design still readily allows to build an asymmetric switching device that qualitatively follows the prediction made with the help of the effective model presented in Eq. (29).

1.9 Parametric encircling and eigenvector flips

To provide an independent proof for the presence of an EP in our experimental setup (see Fig. 3 in the main text), we now make use of the fact that an unambiguous signature of the EP is the state-flip of the instantaneous eigenvectors in the course of a *parametric* EP encircling [11,13,14] (see section 1.7). Correspondingly, our aim is to demonstrate how the two instantaneous Floquet-Bloch modes interchange while traversing our trajectory around the EP, Eq. (34), purely parametrically.

To facilitate this, we firstly note that in the Floquet-Bloch picture an instantaneous eigenstate corresponds to the Floquet-Bloch mode propagating in a periodic waveguide with a fixed modulation frequency detuning δ and amplitude σ. We thus proceed by investigating waveguide configurations at equally spaced points x_n along the path (34), as shown in Supplementary Figs. 7 and 8: Directly at these configurations, the boundary's modulation function is given by $\xi(x) = \sigma_n \sin(\Omega_n x)$, with the instantaneous boundary amplitude σ_n and instantaneous frequency

$$\begin{aligned} \Omega_n &= k_r + 2\delta_0 \left(2\frac{x_n}{L} - 1\right) + \delta_0 + \rho \\ &= k_r + \delta_n \ , \end{aligned} \tag{54}$$

for a waveguide with $L = 25W$. The protocol how to translate the chirped waveguide configuration from Fig. 3 in the main text into the instantaneous values σ_n, Ω_n and δ_n above is, in fact, well known from the literature on chirped laser pulses (see, e.g., chapter 4.6 in [36]). Additionally, also the absorber is periodically continued from the points x_n both in its local shape and strength, maintaining its ability to strongly damp one Floquet-Bloch mode while only weakly affecting the other (see Supplementary Fig. 7a,c). We thus arrive at the conclusion that we can encircle the EP *parametrically* along the same loop (34) that we encircled *dynamically* in our device (Fig. 3), by just concatenating a series of

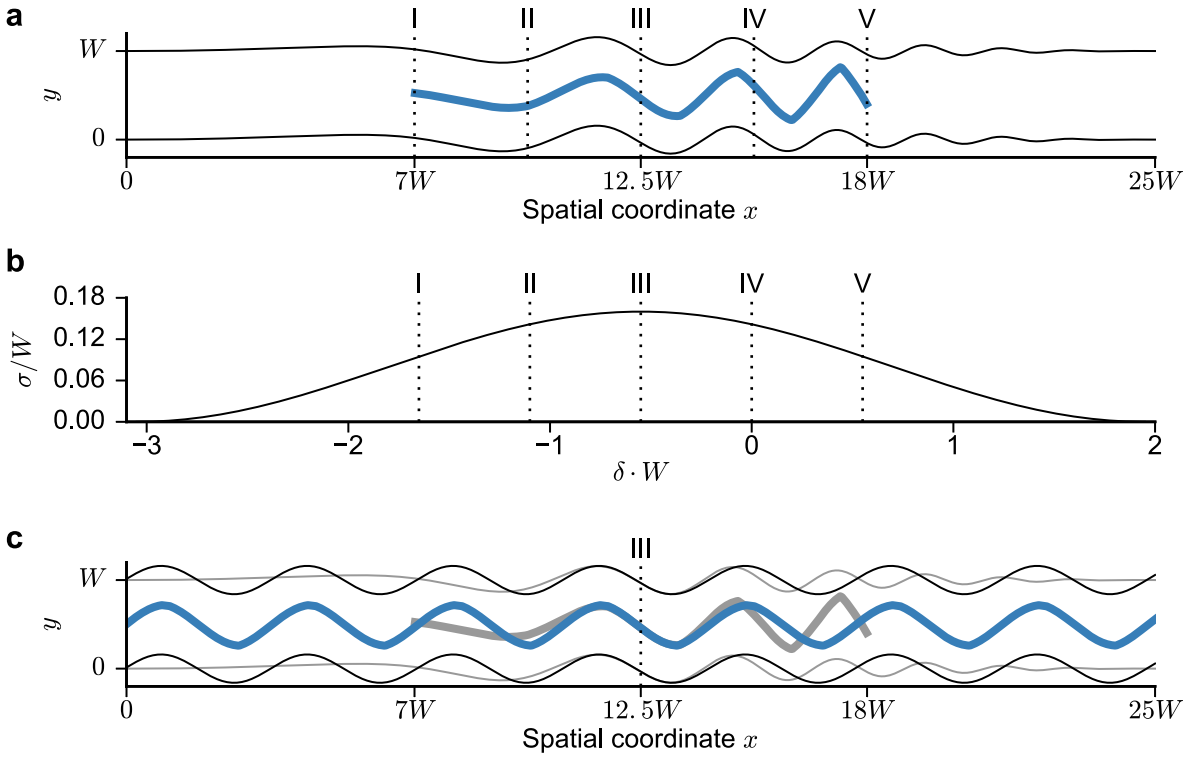

Supplementary Figure 7 | **Instantaneous waveguide configurations.** **a**, Schematic of the experimental waveguide (black lines) corresponding to the setup shown in Fig. 3 in the main text and in Supplementary Fig. 11. The absorber is highlighted by a blue line. **b**, Path taken in (δ, σ)-space to encircle the EP. Vertical dotted lines correspond to configurations I to V at which we manufactured additional waveguides of fixed frequency detuning δ and amplitude σ. Here, $W = 0.05$m denotes the waveguide width. **c**, The instantaneous waveguide configuration III (black line and blue absorber) superimposed on the chirped configuration in **a** (grey line and grey absorber). In the vicinity of the target position $x_{\mathrm{III}} = 12.5W$, both the waveguides and the absorbers coincide.

measurements on periodic waveguides with parameter values distributed along the loop (34).

To implement this protocol also in the experiment we fabricated altogether five periodic waveguide configurations at which we determine the instantaneous Floquet-Bloch eigenmodes. Supplementary Tab. 1 provides the parameters used at the specific points x_n to generate these instantaneous waveguide systems. Since the loop traverses the resonant configuration IV (at which the detuning vanishes), we expect the state-flip of the eigenmodes to occur at this point.

In a periodic system, the instantaneous Floquet-Bloch eigenmodes are defined by their behavior upon the action of the translation operator $\hat{T}_\ell$ that translates a state by a full period ℓ,

$$\begin{aligned} \hat{T}_\ell \phi(x,y) &= \phi(x+\ell, y) \\ &= e^{iK\ell}\phi(x,y)\ , \end{aligned} \tag{55}$$

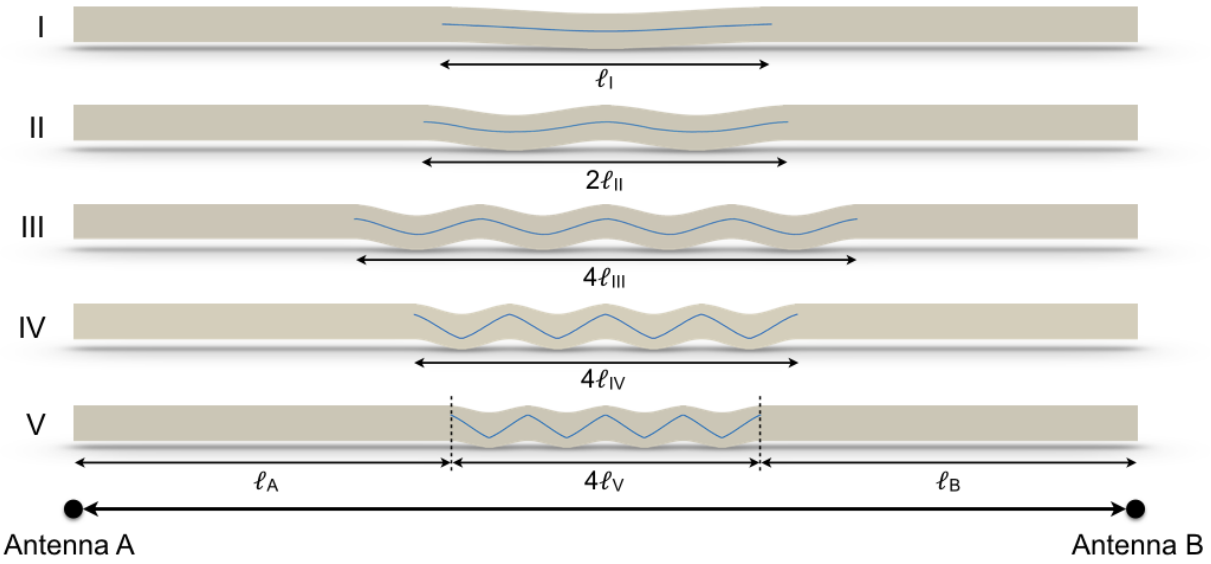

Supplementary Figure 8 | **Waveguide configurations I to V considered in the experiment.** Waveguides with fixed boundary modulation amplitude σ_n and frequency detuning δ_n, as determined by the configurations I to V shown in Supplementary Fig. 7. Antennas are placed at both sides of the waveguide geometry 1.5m apart, the length $\ell_A = \ell_B$ denotes the distance from either antenna to the boundary modulated region which features the periodically continued absorber (blue color). The total length of the periodic segments are chosen to be $m_n\ell_n$, $n = \mathrm{I}, \ldots, \mathrm{V}$, with m_n denoting the number of periods $\ell_n = 2\pi/\Omega_n$ ranging from 1 to 4 (see text for details). The propagation phases accumulated between the center region and the antennas are removed from the experimental data.

configuration n	I	II	III	IV	V
x_n/W	7	9.75	12.5	15.25	18
$\delta_n \cdot W$	-1.65	-1.1	-0.55	0.0	0.55
σ_n/W	0.094	0.1416	0.16	0.1416	0.094

Supplementary Table 1 | **Parameters of the experimental waveguide configurations.** Values for the periodic structures defined in Supplementary Fig. 7 by Roman numerals: The target coordinate x_n, the boundary amplitude σ_n and the linearized detuning δ_n are given in units of the waveguide width $W = 0.05$m.

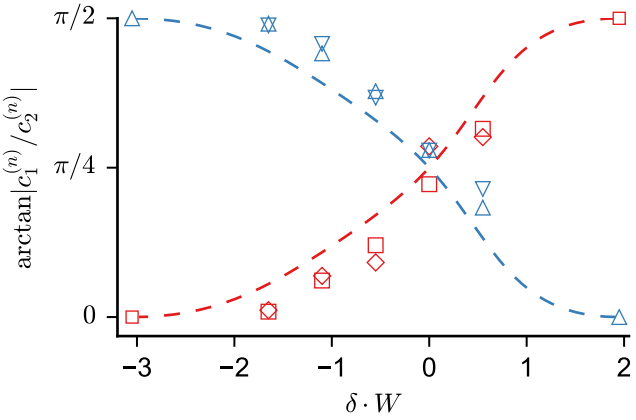

Supplementary Figure 9 | **Transmission matrix eigenvectors.** Ratio of the eigenvector components $c_i^{(n)}$, $i = 1, 2$, where $n = 1$ ($n = 2$) denotes the eigenvector with the higher (lower) transmission eigenvalue τ_n, indicated by red and blue color, respectively. The arctangent is employed to map the ratios onto a finite interval $[0, \pi/2]$. Here we compare the experimentally obtained data (blue downwards pointing triangles, red diamonds) with the predictions of the effective model (dashed lines) and the corresponding numerical simulations (blue upwards pointing triangles, red squares). Triangles and squares at the end points denote solutions which are available analytically (see Eq. (3)).

(see also section 1.2). In terms of the experimentally accessible transmission matrix t for the propagation through m such periods, we can immediately identify

$$t = \hat{T}_\ell^m \ . \tag{56}$$

The Floquet-Bloch eigenmodes in the basis of the two propagating modes (c_1, c_2) are then obtained from the eigenvectors of t[1],

$$\begin{pmatrix} t_{11} & t_{12} \\ t_{21} & t_{22} \end{pmatrix} \begin{pmatrix} c_1^{(n)} \\ c_2^{(n)} \end{pmatrix} = \tau_n \begin{pmatrix} c_1^{(n)} \\ c_2^{(n)} \end{pmatrix} \ , \tag{57}$$

where the coefficients $c_i^{(n)}$ correspond to the ith component of the nth eigenvector, with eigenvalue τ_n. Since the absorber is placed such that one Floquet-Bloch mode is strongly suppressed, $|\tau_1|/|\tau_2| \gg 1$, the eigenvectors are conveniently distinguishable by the absolute value of their eigenvalues (in our experimental data we always have at least $|\tau_1|/|\tau_2| > 6.0$).

In the experiment, we restrict ourselves to waveguide lengths that are four times the period, $\ell_n = 2\pi/\Omega_n$, except for configurations I and II for which the modulated waveguide is one and two periods long, respectively. These values are chosen such that the systems are long enough to ensure that the transmission matrix eigenvectors are sufficiently separated into the Floquet-Bloch modes, but still short enough to allow the measured signal to be above the noise level. The latter requirement necessitates a smaller number of periods for long boundary oscillations.

[1]Please note that in contrast to the main text, the transmission matrix elements are here defined such that t_{nm} determines the transmission from mode m into mode n.

Finally, to demonstrate the state-flip of the instantaneous eigenvectors characteristic for a parametric EP-encircling, we plot the absolute value of the eigenvector component ratio $c_1^{(n)}/c_2^{(n)}$, following both from the experimental as well as from the numerical data, and compare it with the predictions from our effective model (see Supplementary Fig. 9). Indeed, the figure of merit $\arctan|c_1^{(1)}/c_2^{(1)}|$ for the dominant Floquet-Bloch eigenstate (red color) starts close to zero for configuration I, with the eigenvector being almost exclusively in the second sine-mode, $c_2^{(1)} \gg c_1^{(1)}$. At the resonance detuning $\delta = 0$ (configuration IV), a crossing between the dominant and the subdominant eigenmodes is clearly observed. For configuration V, after the eigenstate-flip, the first sine-mode is more dominant than the second one, $c_2^{(1)} < c_1^{(1)}$. Complementing these experimental results with the analytically known eigenstates at the initial and final points of the loop, see Eq. (3), nicely displays the anticipated state-flip. Note that, due to the analytical availability of the states in lossless, straight waveguides with $\sigma = 0$, we have refrained from explicit experimental measurements at the loop endpoints. In addition to the experimental measurements, the state-flip is independently verified also by numerical simulations as well as by the effective model dynamics, showing remarkable agreement.

2 Supplementary figures

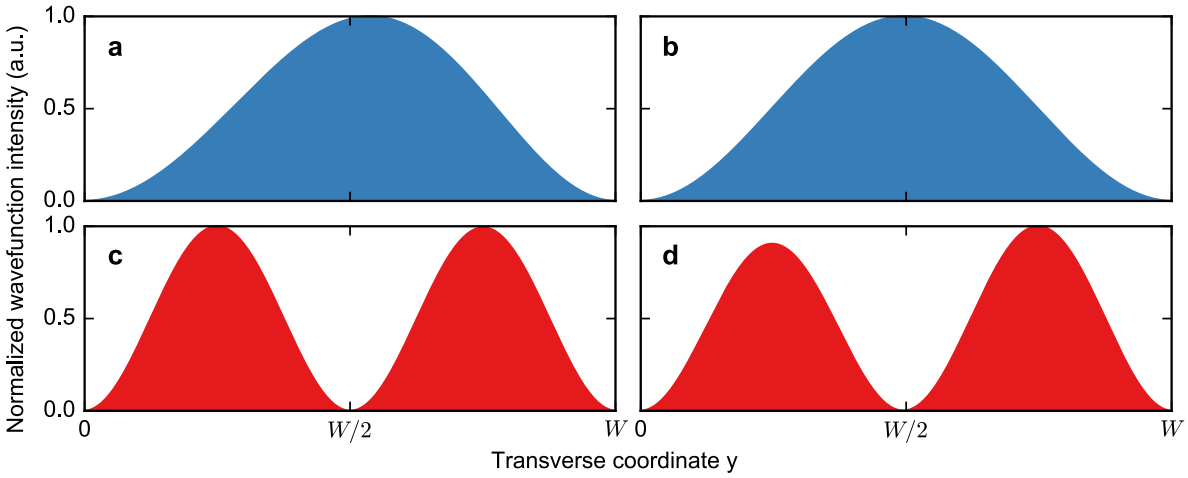

Supplementary Figure 10 | **Modal wavefunction intensities** $|\phi_n(x,y)|^2$ **at the waveguide exit.** Numerically simulated modal wavefunction intensities for a waveguide with a length-to-width ratio $L/W = 100$, obtained at the waveguide exit $x = L$ ($x = 0$) for injection from the left (right). This plot complements the data shown in Fig. 2 in the main text (with **a-d** corresponding to the panels with matching labels in Fig. 2). It is evident that we obtain close to pure modes at the device exits.

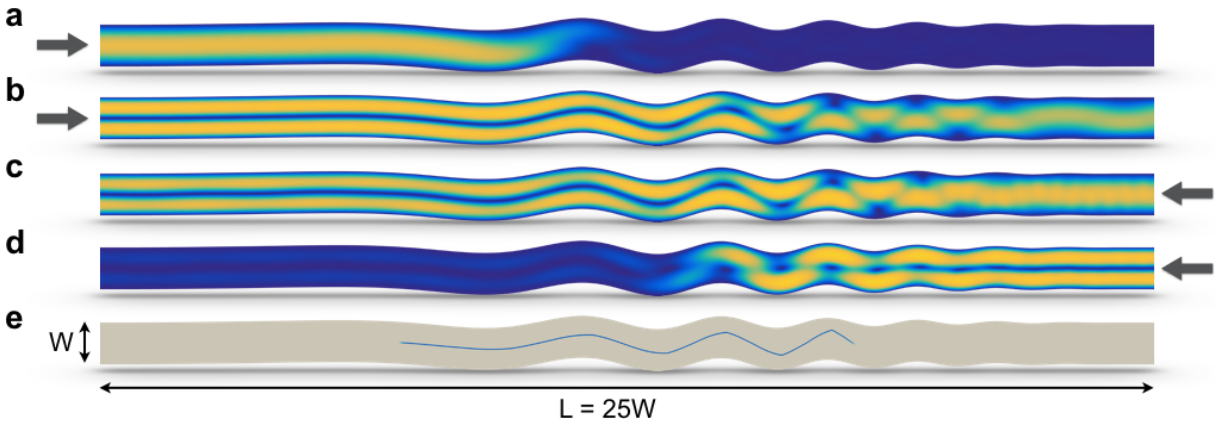

Supplementary Figure 11 | **Modal wavefunction intensities** $|\phi_n(x,y)|^2$**.** Numerically simulated modal wavefunction intensities for a waveguide with a length-to-width ratio $L/W = 25$ (depicted dimensions are to scale). Shown are results for different input modes and injection directions, corresponding to different encircling directions around the EP. Arrows indicate the side from which the waveguide is excited, the first mode is injected in panels **a** and **c**, the second mode in **b** and **d**, respectively. **e**, Plot of the dissipation intensity $\tilde{\eta}(x,y)$. Since the respective reflection intensities R_{nm} are not accessible in the experiment, we have explicitly checked numerically that backscattering is negligible compared to the forward scattering contributions, ensuring that the asymmetry observed in T_{nm} indeed stems from an effective EP encircling. This fact is evident from the respective ratios of the dominant transmission intensity $T_{21} = T'_{12} = 0.66$ vs. all reflection intensities R_{nm}, R'_{nm}, i.e., T_{21}/R_{nm}, T'_{12}/R'_{nm}, which are well above a value of 10^3 (primed quantities correspond to injection from the right side of the waveguide). The following parameters have been used: $kW/\pi = 2.6$, $\sigma_0/W = 0.16$, $\delta_0 W = 1.25$ and $\rho W = -1.8$.

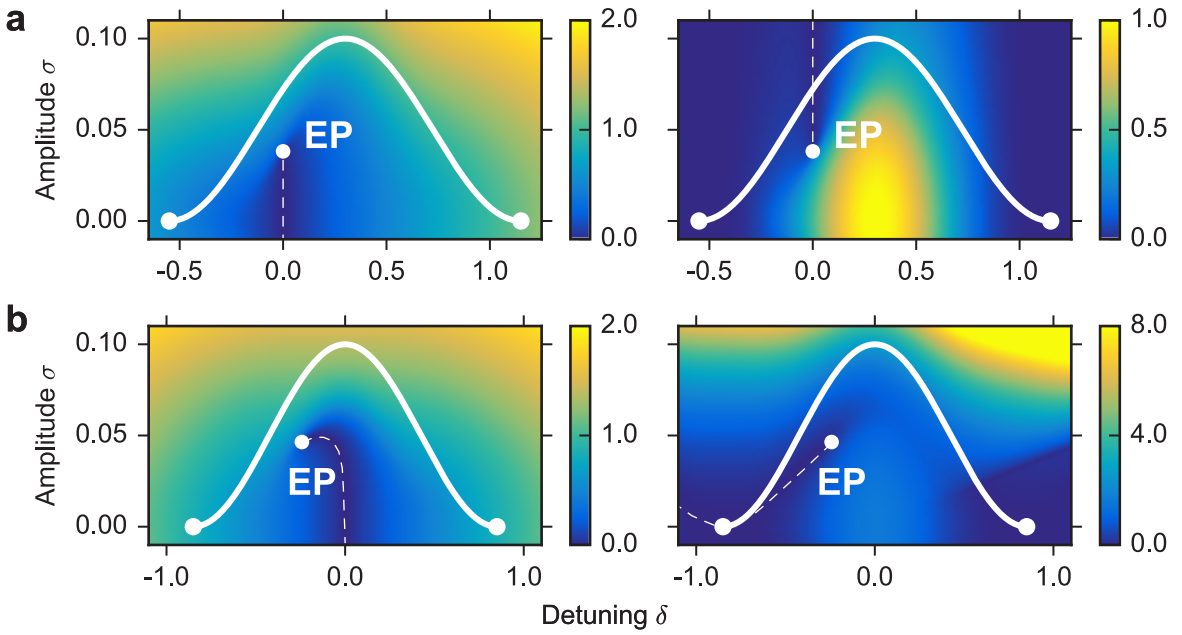

Supplementary Figure 12 | **Parameter space trajectory and eigenvalue sheets.** Paths in parameter space taken in Figs. 4 and 6 (solid white lines in panels **a** and **b**, respectively), on top of heatmaps of the eigenvalue sheets showing $|\mathrm{Re}E_1 - \mathrm{Re}E_2|$ (left column) and $|\mathrm{Im}E_1 - \mathrm{Im}E_2|$ (right column). Start and end points of the trajectories, as well as the EP, are indicated by white dots. The corresponding minima are highlighted by dashed white lines.

References

[34] Jackson, J. D. *Classical Electrodynamics* (Wiley, New York, 1999), 3rd edn.

[35] Seyranian, A. P. & Mailybaev, A. A. *Multiparameter Stability Theory with Mechanical Applications* (World Scientific, 2003).

[36] Asfar, O. R. & Nayfeh, A. H. The application of the method of multiple scales to wave propagation in periodic structures. *SIAM Review* **25**, 455–480 (1983).

[37] Allen, L. & Eberly, J. H. *Optical resonance and two-level atoms* (Dover, New York, 1987).